ACS APPLIED MATERIALS & INTERFACES

www.acsami.org

Research Article

Unraveling the Intrinsic Biocidal Activity of the SiO_2−Ag Composite against SARS-CoV-2: A Joint Experimental and Theoretical Study

Marisa Carvalho de Oliveira,* Marcelo Assis, Luiz Gustavo Pagotto Simões, Daniel Tamassia Minozzi, Renan A. P. Ribeiro, Juan Andrés, and Elson Longo

Cite This: *ACS Appl. Mater. Interfaces* 2023, 15, 6548−6560

Read Online

ACCESS | Metrics & More | Article Recommendations | Supporting Information

ABSTRACT: The COVID-19 pandemic has emerged as an unprecedented global healthcare emergency, demanding the urgent development of effective materials to inactivate the SARS-CoV-2 virus. This research was planned to disclose the remarkable biocidal activity of SiO_2−Ag composites incorporated into low-density polyethylene. For this purpose, a joint experimental and theoretical [based on first-principles calculations at the density functional theory (DFT) level] study is performed. Biological assays showed that this material eliminates*Staphylococcus aureus*and SARS-CoV-2 virus in just 2 min. Here, we investigate a previously unexplored process that we postulate may occur along the O_2 and H_2O adsorption and activation processes of pure and defective SiO_2−Ag surfaces for the generation of reactive oxygen species (ROS). The obtained results help us to predict the nature of ROS: superoxide anion radicals, $^{\bullet}O_2^-$, hydroxyl radicals, $^{\bullet}OH$, and hydroperoxyl radicals, $^{\bullet}HO_2$, that destroy and degrade the structure of the SARS-COV-2 virus. This is consistent with the DFT studies, where the energetic, electronic, and magnetic properties of the intermediates show a feasible formation of ROS. Present findings are expected to provide new insights into the relationship among the structure, property, and biocidal activity of semiconductor/metal SiO_2−Ag composites.

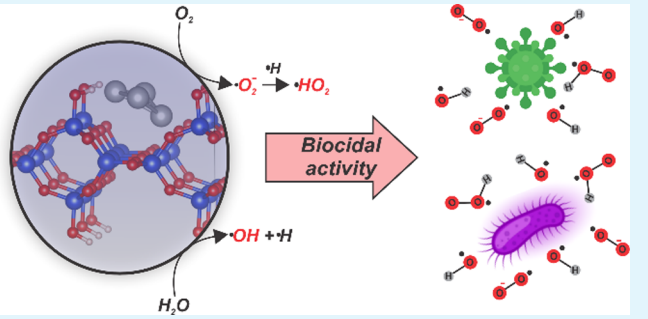

KEYWORDS: *SiO_2−Ag, DFT calculations, ROS, SARS-CoV-2, biocide*

1. INTRODUCTION

Pathogens such as bacteria, fungi, and viruses have posed an enormous threat to mankind.[1] An example is the ongoing worldwide COVID-19 pandemic caused by the severe acute respiratory syndrome-related coronavirus 2 (SARS-CoV-2), which emerged as a threat to public health and raised people's awareness of the best practices to prevent the spread of these microorganisms. For this reason, scientific and technological innovations have been the focus of researchers who aim to develop effective biocidal technologies to provide a benign and sustainable approach to prevent infections in daily life. While there is an urgent need for the effective treatment of these outbreaks through the use of vaccines, the emergence of multiple SARS-CoV-2 variants of concern reinforces the importance of developing safe and effective biocidal materials for their functionalization on surfaces capable of killing microorganisms upon contact.[2−6]

Nanostructured materials such as metals, for example, Ag, Au, Zn, Cu, and Fe, and metal oxide semiconductors, for example, CuO, ZnO, Fe_2O_3, CeO_2, and TiO_2, have demonstrated biocidal activity.[7−12] These nanomaterials exert their effects by affecting the integrity of the bacterial cell membrane, releasing metal cations, leading to oxidative stress via the generation of reactive oxygen species (ROS) on the material surface, and inhibiting enzyme activity and DNA synthesis. Along with oxidative stress, the activation of both O_2 and H_2O molecules plays a key role in these processes, as they act as progenitor species to generate ROS such as $^{\bullet}O_2^-$ and $^{\bullet}OH$. These ROS are involved in a chain reaction with the formation of other highly reactive oxidants, for example, singlet oxygen, $^1O_2$, hydroperoxyl radical, $^{\bullet}HO_2$, or hydrogen peroxide, H_2O_2, to initiate the desired oxidation reactions associated with biocidal activity.[13] Because activated O_2 and H_2O molecules have such an important practical effect, their research is a meaningful subject.

Silica (SiO_2)-based materials have highly versatile structural properties that are interesting platforms or a plethora of applications due to their biocompatibility, nontoxicity, chemical inertness, and very high specific surface area. The major advantage is its high degree of functionalization associated with the presence of a huge quantity of silanol

Received: November 22, 2022
Accepted: January 11, 2023
Published: January 25, 2023

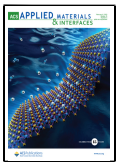

https://doi.org/10.1021/acsami.2c21011
ACS Appl. Mater. Interfaces 2023, 15, 6548−6560

groups on the surface, providing the possibility of loading/release of different kinds of drugs.[14] It is well known that the integration of noble Ag nanoparticles in semiconductors is an effective strategy to enhance biocidal activity due to the synergic effects on the metal/oxide interface. Prospects for the use of these materials in various areas of modern technology require comprehensive studies of their properties and applications.[15−19] On the other hand, polymer−inorganic hybrid nanomaterials by two or more components connected at the nanometer scale are attractive because they combine the intrinsic properties of both materials with additional properties resulting from synergistic effects.[20]

The SiO_2−Ag composite takes advantage of the distinctive properties of Ag as a potent antimicrobial agent[21−23] and the porous inorganic 3D network structure of SiO_2, resulting in fast mass transport, high thermal and mechanical stability, a large specific surface area, biocompatibility, and easy functionalization.[24−27] Over the last few years, our research group has reported that the SiO_2−Ag composite with anti-SARS-CoV-2 properties is a versatile, low-cost, and tolerant additive to functionalize textiles and surfaces, representing a safe alternative for its application and the prevention of microbial proliferation and transmission. Indeed, the experimental results indicated that the as-fabricated samples exhibited a high antibacterial activity toward*E. Escherichia coli*and*Staphylococcus aureus*, as well as an antiviral activity against SARS-CoV-2.[28,29] The main advantage for such composite is the reduced time required to eliminate virus and bacteria when compared to recently developed coatings containing silver oxide (Ag_2O) particles in a silicate matrix on glass.[30]

Current measurement processes, such as spectroscopy techniques, fluorescence-dependent methods, electron spin resonance approaches, etc., cannot characterize the ROS activity with spatiotemporal information revealing the correlation between the activity of composites and their specific composition and surface structure. In addition, there is the question of how to promote the electron transfer process for more effective O_2 and H_2O activation. Therefore a more complete understanding of the production and distribution of ROS on the surface of the SiO_2−Ag composite is needed, and a critical discussion is required for clarifying the mechanism of biocidal activity and improving their efficiency.

In this work, we carried out the synthesis of the SiO_2−Ag composite incorporated into low-density polyethylene (LDPE) and characterized it by X-ray diffraction (XRD), Fourier transform infrared (FTIR) spectroscopy, and thermogravimetric analysis (TG/DTA). Contact angle (CA) measurements are performed to investigate its antibacterial activity toward *S. aureus* and SARS-CoV-2 virus. Polyethylene is the most used polymer worldwide in the development of new technologies based on plastics, representing more than 34% of day-to-day activities of modern society.[31,32] In addition, as there are no articles on O_2 and H_2O activation concerning biocidal activity, first-principles calculations within the density functional theory (DFT) framework were employed to obtain atomic-level information on the geometry, energetics, and electronic structure of SiO_2−Ag surfaces. In addition, to understand the formation and evolution of ROS from the new perspective of energy and charge transfer processes, its interactions with O_2 and H_2O are explored for the first time. Overall, the aim of our contribution is twofold. First, the key variables that determine the wetting of Ag nanoparticles on the SiO_2 semiconductor substrate were investigated in detail. Second, the mechanism of biocidal activity was rationalized from the perspective of ROS formation process on the composite surface. These objectives will allow us to draw interesting conclusions about the beneficial effects of the SiO_2−Ag composite and understand how the Ag clusters act on the SiO_2 surface. As a proof of concept, we showed that first-principles calculations can be a useful tool in additional studies since, in conjunction with experimental techniques, we could obtain a more complete picture of how ROS evolve over time and promote their further application in polymer SiO_2−Ag-based materials.

The rest of the article is divided into three more sections. The next section describes the synthesis, experimental characterization, computational details, and model systems. In the Results and Discussion section, energetic and structural aspects as well as electronic band structure data are detailed and analyzed. The article ends with a summary of our findings and conclusions.

2. EXPERIMENTAL SECTION

2.1. Synthesis. The SiO_2−Ag composite was synthesized as described in previously published articles by our group.[28,29] The LDPE was donated by the Braskem company (Santo André, Brazil). An amount of 1.0% by weight of the SiO_2−Ag composite was added to the LDPE granules, and another 1.0% was mechanically mixed. Then, the LDPE pellets mixed with SiO_2−Ag were heated at 150 °C for 1 h. Particle dispersion was performed using an ULH 700S ultrasonicator in oil at 150 °C for 30 min. The melted composite was poured into a mold at a temperature of 125 °C and pressed at 10 kg/cm^2 for 2 min using a hot press (20 tons). Subsequently, the pellets were reheated at 125 °C in a 50 mL stainless steel syringe with a 1/16 in. Swagelok tip as an extrusion die. Shear extrusion was applied to the composite by pressure through a cylindrical stainless-steel channel with a diameter of 1 mm and a length of 50 mm after heating at 125 °C for 1 h. The tape extruded in the channel was cooled to room temperature using an air blower.

2.2. Characterizations. The composite materials were characterized by XRD on a D/Max-2500PC diffractometer (Rigaku, Tokyo, Japan) with Cu Kα radiation (λ = 1.5406 Å) in the 2θ range of 10−70° and at a scanning speed of 1° min^{-1}. The diffractograms were deconvoluted using the Voigt area function in the PeakFit v4 program. For the FTIR spectra, a Bruker Vector 22 FTIR spectrophotometer was used in the range of 400−4000 cm^{-1} with the acquisition of 32 scans. The thermal stability analysis of the samples was performed on a NETZSCH STA 409 TG/DTA at a temperature of 25 to 700 °C and a heating rate of 10 °C min^{-1}, in an O_2 atmosphere with a flow rate of 50 mL min^{-1}. Contact angle analyses were carried out based on the sessile drop method in static mode using an F4 Ramé-hart series model 260 goniometer. A drop of 5 μL of distilled water was deposited on the surface of each sample, and the angle formed between the drop and the polymer surface was determined using the DROPImage Advanced software.

2.3. Bactericidal and Antiviral Tests. Colony samples of *S. aureus* ATCC 6538 P were grown over two nights on Mueller−Hinton agar (MH2) plates and were resuspended in a test tube containing MH2 broth. The inoculum was standardized by transferring the colonies to a 0.9% saline solution until reaching 0.5 on the McFarland scale. The turbidity (expressed in optical density) was obtained in a spectrophotometer (λ = 620 nm), representing approximately 1.5 × 10^8 CFU. A 1:10 dilution in 0.9% saline was then performed so that the initial inoculum was 1.0 × 10^7 CFU/mL. Antimicrobial activity was then performed according to the standard test methodology described in ISO 21702—Measurement of antibacterial activity on plastics and other non-porous surfaces.[33] A volume of 100 μL of *S. aureus* ATCC 6538 P solution (at a concentration of 1.0 × 10^7 CFU/mL) was inoculated in triplicate on

https://doi.org/10.1021/acsami.2c21011
ACS Appl. Mater. Interfaces 2023, 15, 6548−6560

the surface of the samples (5 × 5 cm) and covered with sterile plastic film to ensure distribution of the bacterial solution throughout the entire surface area of the specimen. The samples were then incubated at 37 °C for 24 h. After incubation, the inoculum was recovered with 10 mL of soy casein digested lecithin polysorbate broth , followed by serial dilution in phosphate-saline buffer. Each dilution was seeded on MH2 agar and incubated at 37 °C for 24 h. The CFU/cell quantity was determined after incubation.

Virucidal tests were performed to assess the inactivation potential of the SARS-CoV-2 virus in a similar way as described above, following ISO 21702:2019—Measurement of the antiviral activity on plastics and other non-porous surfaces.[34] Tests were performed on three independent occasions in triplicate. Samples with standardized dimensions of 5 × 5 cm were placed individually in Petri dishes. The material was exposed to the viral solution, where the SARS-CoV-2 viral solution is added so that it covers the entire surface of the material, and after this contact, it is incubated for 2 to 10 min. After this process, it is neutralized and serially diluted. The viral titer is then measured using the infectious tissue culture dose 50 ($TCID_{50}$) methodology. The reduction of SARS-CoV-2 copies was quantified after the respective incubation times. The results are expressed in comparison of the virucidal action against the reduction of viral copies of the SARS-CoV-2 stock solution with a "non-virucidal" material (blank/control) and the "active" material so that it is possible to calculate the percentage of viral inactivation, represented by the Log_{10} reduction of $TCID_{50}$. The cytopathic effect was analyzed in an inverted microscope after an incubation period of 72 h in an oven at 37 °C with 5% CO_2, using the Spearman & Karber method, and the viral titer quantification data obtained in the incubation process were applied to the end-point-dilution methodology, in which the inoculation of successive decreasing dilutions in viral suspension applied to the cells is evaluated; thus, it is possible to identify the cytopathic effect in 50% of the inoculated cultures.[35] In this way, visual confirmation of the cytopathic effect of the SARS-CoV-2 strains against the Vero ATCC CCL-81 cell is obtained. To improve the reliability of the result, a correction factor related to the dilution volume of the virus (SARS-CoV-2) used in each $TCID_{50}$ assay was applied.[36] To determine the viral inhibition index, the logarithmic difference between the control group and the active group was used.

The antimicrobial data were analyzed using the Shapiro−Wilk test, analysis of variance by the Brown−Forsythe test, analysis with a one-way RM ANOVA to verify the parametric or non-parametric nature of the data, and a post-hoc test of Tukey's multiple comparisons. Results are presented as the median with upper and lower quartiles: Me [Q1; Q3]. Statistical significance was set at $p < 0.05$.

The aging of the samples was carried out through continuous ultraviolet irradiation (600 h of exposure). The aging process followed the guidelines described in ISO 4892-2:2013 Plastics—Methods of exposure to laboratory light sources—Part 2: Xenon-arc lamps.[37]

2.4. Computational Methods and Model Systems. In this study, the structural and electronic features of the SiO_2−Ag composite were studied by first-principles calculations at the DFT level. The hybrid functional B3LYP augmented with two- and three-body contributions to the long-range dispersion energy (B3LYP-D3)[38] was employed, as implemented in the CRYSTAL17 code.[39] The Si, O, and H centers were described by an all-electron GTO basis set defined as 66-21G(d), 6-31G(d), and 31G(p), respectively, while the Ag centers were described by the effective core pseudopotential HAYWSC-311d31G.[40,41] The evaluation of the Coulomb and exchange series was truncated to 10^{-7} for the Coulomb overlap tolerance, 10^{-7} for the Coulomb penetration tolerance, 10^{-7} for the exchange overlap tolerance, 10^{-7} for the exchange pseudo-overlap in the direct space, and 10^{-14} for the exchange pseudo-overlap in the reciprocal space. The condition for the SCF convergence was set to 10^{-7} a.u. for the total energy difference between two subsequent cycles. Furthermore, default thresholds for geometry optimization within the CRYSTAL code were used for all atoms: while the maximum and root-mean-square (rms) forces were set to 0.000450 and 0.000300 a.u., the maximum and rms atomic displacements were set to 0.001800 and 0.001200 a.u., respectively. The *k*-space sampling for the geometry optimization included a 3 × 3 × 1 Monkhorst−Pack mesh.

The theoretical description of amorphous SiO_2 is challenging given the difficulty of representative models to describe different silanol groups (Si−OH). In particular, they need to properly represent structural defects as reactive centers on the exposed surfaces.[42−47] In this context, Ugliengo and co-workers conducted a series of theoretical studies to obtain a representative model using the edingtonite SiO_2 bulk, as depicted in Figure S1 (Supporting Information), which contains the building block Y formed by the connections between neighboring [SiO_4] clusters.[48−51] In this model, the SiO_2 surface is represented by a slab along the (100) surface (Figure S2—Supporting Information) containing superficial [SiO_4] clusters (Figure S2a—Supporting Information) with two non-equivalent oxygen groups, since the oxygen atoms labeled as 1−3 are equivalent in symmetry and two-fold coordinated as in the SiO_2 bulk, while the outermost atom is O_4. Therefore, all outermost oxygen atoms were hydroxylated to generate silanol Si−OH groups (Figure S2b−Supporting Information) with a density of 2.2 isolated hydroxyls per nm^2, as experimentally observed in dehydrated SiO_2[52,53] (1−2 OH per nm^2) and demonstrated by our previous FTIR results, which confirmed the presence of superficial Si−OH groups.[28]

Additionally, the (100) SiO_2 slab was expanded as a 2 × 2 supercell model established with 72 atoms ($Si_{20}O_{44}H_8$), as shown in Figure S3a (Supporting Information). To take into account the role of superficial defects, two additional models were considered. In models 1 (V_H—71 atoms) and 2 (V_{OH}—70 atoms), a −H atom and a −OH group were respectively removed (see Figure S3b—Supporting Information).

To simulate the SiO_2−Ag composite, the three models were employed, with the Ag nanoparticles being represented by an Ag_4 cluster with D_{2h} symmetry, following the work by Chen et al.[54] based on the adsorption of small Ag clusters on graphene. Figure S4 (Supporting Information) shows the top and side views of the selected models named A, B, and C, with a total number of atoms of 76, 75, and 74, respectively.

The interaction energy (E_{int}) of the composite was calculated according to the equation below

$$E_{int} = E^{slab}_{SiO_2-Ag} - E^{slab}_{SiO_2} - E^{cluster}_{Ag} \quad (1)$$

where $E^{slab}_{SiO_2-Ag}$ is the total energy of the SiO_2−Ag composite slab, $E^{slab}_{SiO_2}$ is the total energy of the isolated optimized SiO_2 slab, and $E^{cluster}_{Ag}$ is the total energy of the isolated Ag_4 cluster.

To provide detailed mechanistic insights into the O_2 and H_2O adsorption processes on the surfaces of SiO_2−Ag models (A, B, and C), the energetics of different adsorption sites was investigated by calculating the adsorption energies according to the following equations

$$E_{ads} = [E^{slab}_{SiO_2-Ag+O_2/H_2O} - (E^{slab}_{SiO_2} + E_{O_2/H_2O}) + E_{BSSE}] \quad (2)$$

$$E_{BSSE} = (E^{frozen}_{SiO_2-Ag} - E^{frozen}_{SiO_2-Ag+ghost]}) + (E^{frozen}_{O_2/H_2O} - E^{frozen}_{O_2/H_2O+ghost}) \quad (3)$$

where $E^{slab}_{SiO_2-Ag+O_2/H_2O}$ is the total energy of the optimized SiO_2−Ag slab with adsorbed O_2/H_2O molecule, $E^{slab}_{SiO_2}$ is the total energy of the isolated optimized SiO_2−Ag slab, and $\mathbf{E_{O_2/H_2O}}$ is the total energy of O_2 and H_2O molecules in the gas phase. The basis set superposition error (BSSE) was calculated considering the two separated moieties (slab + O_2/H_2O) frozen in the minimum adsorption configuration, with and without ghost functions, respectively. Spin polarization was considered in the case of open-shell systems, while geometry optimization was performed without any symmetry constraints to the upper side of the SiO_2 models. More details on the DFT calculations are given in the Supporting Information.

https://doi.org/10.1021/acsami.2c21011
ACS Appl. Mater. Interfaces 2023, 15, 6548−6560

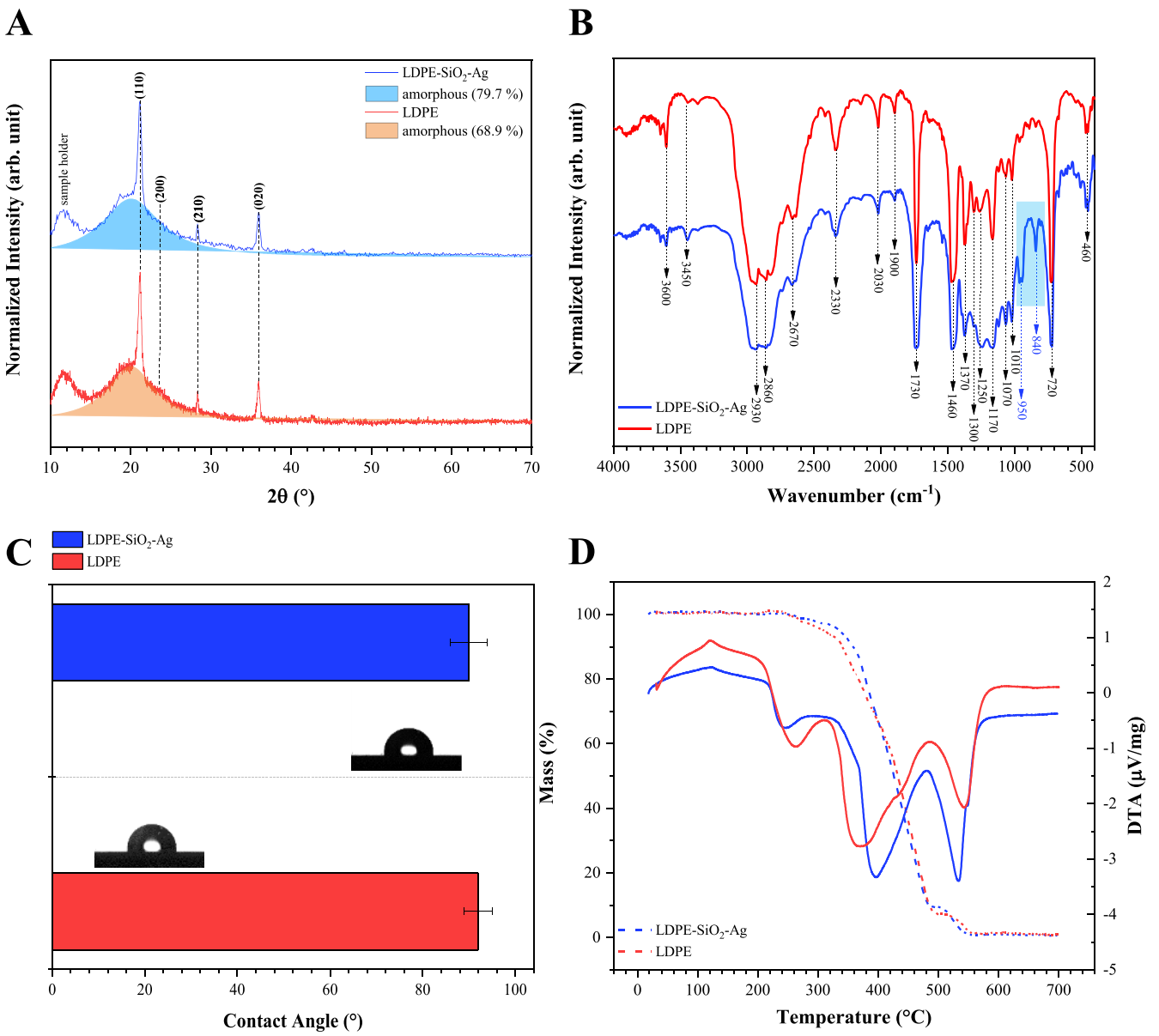

Figure 1. (a) XRD patterns, (b) FTIR spectra, (c) WCAs, and (d) TG/DTA measurements of the LPDE and LPDE−SiO_2−Ag samples.

3. RESULTS AND DISCUSSION

3.1. Experimental Analysis. Figure 1a shows the diffractograms for the LDPE and LDPE−SiO_2−Ag samples. The crystallographic (110), (200), (210), and (020) planes referring to the orthorhombic phase of the LDPE are indexed to the samples.[55] In addition, a large amount of amorphous material is observed in both structures. To quantify this amount, a deconvolution of the amorphous band was performed using the Voight area function,[56] resulting in percentages of 68.9 and 79.7% of amorphous phase for the LDPE and LDPE−SiO_2−Ag samples, respectively (Figure 1a). The amount of amorphous phase increases in the LDPE−SiO_2 composite due to the presence of distorted [SiO_4] clusters of SiO_2−Ag particles capable of breaking the long-range symmetry of the composite, thus favoring the amorphous material formation.[28] The XRD analysis was complemented with FTIR measurements, as shown in Figure 1b, where the bands associated with C−H bonds of both amorphous and crystalline phases are observed.[55] It is important to note that the bands located at 840 and 950 cm^{-1} found in the LDPE−SiO_2−Ag sample are related to the O−Si−O bending motion, which confirms the successful incorporation of SiO_2−Ag particles into the LDPE. Water contact angle (WCA) analysis was conducted for both samples, with no significant differences being found between them (Figure 1c). The TG/DTA profiles did not change with the addition of SiO_2−Ag particles (Figure 1d) as well. Therefore, it can be suggested that the manufacture of composite materials with the addition of these particles does not provoke drastic changes.

Figure 2a shows the bactericidal activity of the composite material against the Gram-positive bacterium *S. aureus*. An analysis of the results renders that LDPE−SiO_2−Ag samples reduce the amount of initial bacteria on a scale of 4 $\log_{10}$ (99.99%) with respect to LDPE. Similarly, 99.99% elimination is also obtained (i.e., 4 $\log_{10}$ reduction) for the copies of SARS−CoV−2 (Figure 2b) in just 2 min. Tests to analyze pathogen elimination in 10 min were slightly better than those performed with an elimination time of 2 min. Antimicrobial

https://doi.org/10.1021/acsami.2c21011
ACS Appl. Mater. Interfaces 2023, 15, 6548−6560

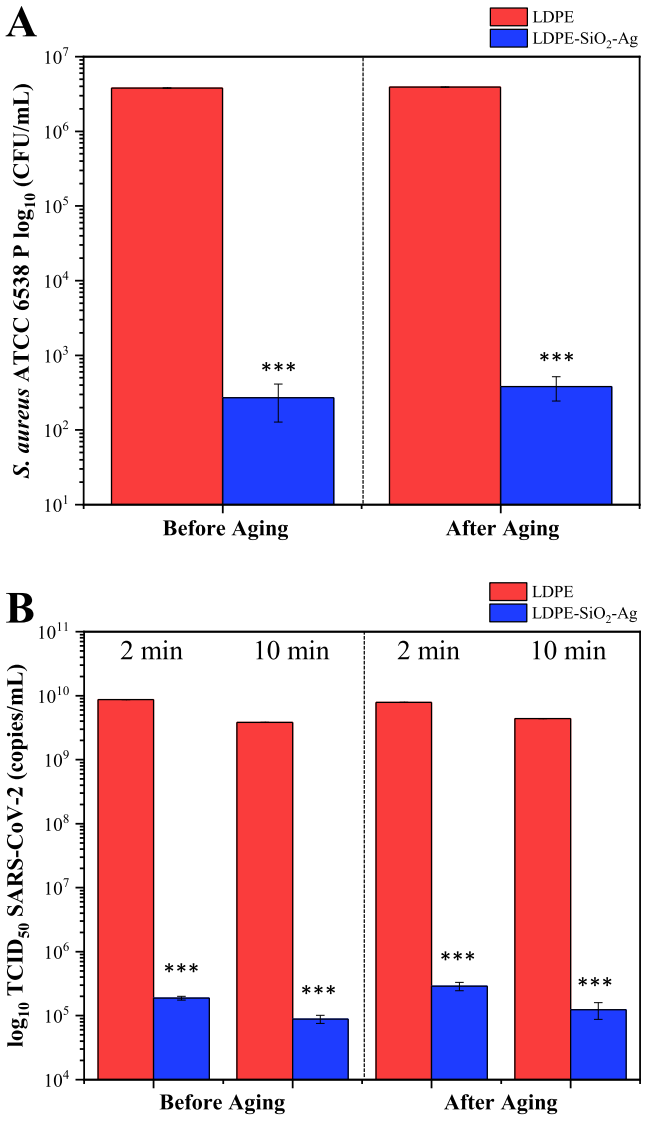

Figure 2. ISO-based antimicrobial testing using (a) *S. aureus* and (b) SARS-CoV-2 before and after aging. *p < 0.5; **p < 0. ***p < 0.001; ****p < 0.005. The results are presented as the median with the upper and lower quartiles: Me [Q1; Q3].

tests were carried out after the aging of the sample specimens, showing results very close to the initial ones before aging (Figure 2).

3.2. DFT Results. *3.2.1. Structure and Stability.* The role of superficial defects in the structural, energetic, and electronic properties of the SiO_2 models was analyzed, and the corresponding results are summarized in Table 1. As it can be seen, the creation of hydrogen and hydroxyl vacancies generates local structural disorder alongside the exposed surface, increasing the Si−O bond length in the defective cluster, while the neighboring clusters remain almost stable due to the small variations in Si−O and O−H bond lengths. Indeed, by comparing the $[SiO_4H]$ clusters for the pure and defective models, the Si−O and O−H bond lengths are almost identical, whereas the remaining Si−O bonds for both $[SiO_4\cdots V_H]$ and $[SiO_3\cdots V_{OH}]$ are larger than those of the pure model, confirming the local structural disorder in the defective clusters.

Table 1. Values of the Bond Lengths for Pure and Defective SiO_2 Surface Models

model	clusters	bond lengths (Å)
pure	$[SiO_4H]$	Si−O = 1.626 (4×)
		O−H = 0.963 (1×)
VH	$[SiO_4\cdots VH]$	Si−O = 1.665 (4×)
	$[SiO_4H]$	Si−O = 1.625 (4×)
		O−H = 0.963 (1×)
VOH	$[SiO_3\cdots VOH]$	Si−O = 1.653 (2×)
		Si−O = 1.645 (1×)
	$[SiO_4H]$	Si−O = 1.626 (4×)
		O−H = 0.963 (1×)

The structure of the Ag_4 cluster was optimized to attach to the surface of SiO_2, yielding SiO_2−Ag_4. The structural properties of the SiO_2−Ag composite represented by models A, B, and C were analyzed in detail, as summarized in Figure S5 (Supporting Information). An analysis of the results renders that for model A the Si−OH bonds neighboring the Ag_4 cluster rotate to form an H−Ag bond of approximately 2.421 Å, resulting in an enlargement of O−H bonds of 0.990 Å compared to the value of other silanol groups (0.964 Å). The Ag_4 cluster also interacts with the in-plane oxygen atoms with a distance of 2.848 Å, while the mean Ag−Ag bond distance is 2.731 Å. This value is similar to that reported in the theoretic study of small Ag clusters adsorbed on graphene.[54] On the other hand, the presence of superficial defects induces the rotation of the Ag_4 cluster closer to the defect centers. For model B, the Ag atoms interact with the $[SiO_4\cdots V_H]$ center at a distance of 2.257 Å, and also with superficial H (2×) and O atoms at 2.716, 2.879, and 2.759 Å, respectively, with a mean Ag−Ag bond distance of 2.759 Å. Finally, for model C, in which the Ag cluster interacts with $[SiO_3\cdots V_{OH}]$ at a distance of 2.467 Å, displays superficial H atoms, at distances of 2.864 and 2.957 Å, and with a mean Ag−Ag bond length of 2.778 Å. Therefore, the presence of intrinsic defects on SiO_2 surfaces induces a stronger interaction between the defect center and the Ag atoms, causing an enlargement of the remaining Ag−Ag bond lengths.

To understand the electronic structure of the pure, hydrogen deficient, and hydroxyl-deficient SiO_2 models, as well as the SiO_2−Ag models, the total and projected density of states (DOS) were calculated (see Figures S6 and S7—Supporting Information, respectively).

After analyzing the electronic properties, it was noticed that the valence band (VB) was formed by oxygen 2p orbitals for all models; while for the conduction band (CB), only empty 3s orbitals from Si. The overall electron density of unoccupied states was increased if the Ag atoms adhered to SiO_2 due to the participation of 4d, 5s, and 5p orbitals in the CB (Ag_4 cluster). As a result, new sets of electronic states in the bang gap are formed. The creation of hydrogen and hydroxyl vacancies decreases the band gap value to 5.23 (V_H) and 3.56 eV (V_{OH}), respectively, in comparison with the wide band gap of the pure model (8.70 eV). For model A, the inclusion of Ag_4 clusters results in a metallic system since the valence states of Ag cross the Fermi level. The high electronegativity of Ag (χ = 2.4) facilitates the interaction between the Ag_4 cluster and SiO_2, promoting the electronic transfer can occur from the CB. Furthermore, the creation of superficial defects in models B and C was observed in the vicinity of the Fermi level, generating half-metallic systems, that is, systems with a metallic

https://doi.org/10.1021/acsami.2c21011
ACS Appl. Mater. Interfaces 2023, 15, 6548−6560

spin-up channel while the spin-down channel keeps following the semiconductor behavior.

The results show a decrease in the bandgap energy for SiO_2−Ag, which assists the electron injection from the Ag_4 cluster to the CBs. This is consistent with the fact that the Fermi energy level of the Ag_4 cluster has been positioned just below the CB, producing a Schottky barrier at the interface of SiO_2. This behavior can be related to the delocalization associated with the Ag clusters as stated in the jellium model. This reasoning was proposed in previous studies[57,58] and more recently by Huerta-Aguilar et al.[59] to explain the photocatalytic and antibacterial properties of $ZnFe_2O_4$−Ag nanoparticles.

The positions of the VB and CB potentials were calculated using the following equations

$$E_{VB} = \chi - E_e + \frac{1}{2}E_{gap} \quad (4)$$

$$E_{CB} = E_{VB} - E_{gap} \quad (5)$$

$$\chi = [\chi(Si)^a\chi(O)^b\chi(H)^c\chi(Ag)^d]^{1/a+b+c+d} \quad (6)$$

where E_{CB} is the CB potential, E_{VB} is the VB potential, χ is the electronegativity (a, b, c, and d are the number of each atomic species in the proposed model), E_e is a constant with value of 4.5 eV, and E_{gap} is the calculated band gap. The calculated values of χ were 6.46, 6.45, and 6.43 eV for models A, B, and C, respectively.

The determination of the potentials for the VB and CB, associated with the redox potentials of charge carriers during surface reactions, allows one to predict which reactions can occur on the surface by comparing the surface band edges and the potential formation of different ROS.[60,61] The VB edge potentials were calculated (see Figure 3), and as it can be seen,

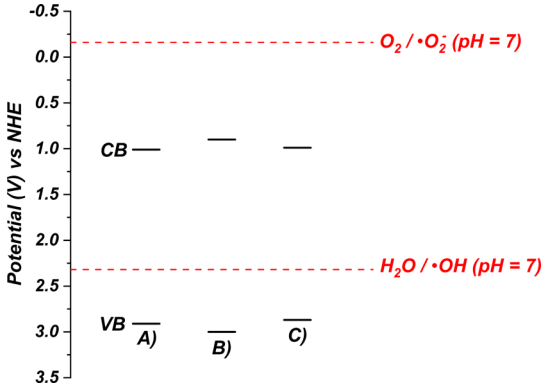

Figure 3. Calculated values of the VB- and CB-edge potentials for the models A, B, and C.

VB potentials are more positive than those of $H_2O/^{\bullet}OH$ (2.33 V vs NHE at pH = 7), which suggests that the interaction between H_2O and holes favors the generation of $^{\bullet}OH$. In contrast, the CB edge potentials are more positive than those of $O_2/^{\bullet}O_2^-$ (−0.16 V vs NHE at pH = 7), which indicates that the electron transfer to adsorbed molecular oxygen, O_2, to render $^{\bullet}O_2^-$ is more difficult to occur.

From now on, the energetics and electronic features of the SiO_2−Ag models are investigated as functions of the O_2 and H_2O adsorption processes responsible for the generation of ROS species. In previous experimental investigations,[28,29] it was observed that h^+, $^{\bullet}OH$, and $^{\bullet}HO_2$, are the reactive species acting in the mechanism for virus elimination.

3.2.2. O_2 Adsorption Process and ROS Generation Mechanism. Figure 4 shows the selected values of O−O, Ag−O, and H−O distances and E_{ads} of the optimized structures of the adsorption process of O_2 on the three SiO_2−Ag models.

The relative values of E_{ads} follow the order A > C > B. Due to the formation of Ag−O and O−H bonds, the A model corresponds to a chemisorption process, while in the defective models (B and C), a physisorption process can be detected with a weak interaction between the O_2 molecule and the Ag_4 cluster. This fact can be associated with the very strong interaction between the Ag_4 cluster and the defective $[SiO_4\cdots V_H]$ and $[SiO_3\cdots V_{OH}]$ states present on the SiO_2 surface. In other words, these vacancies can work as the electron trapping sites, facilitating the formation of $^{\bullet}O_2^-$ and thereby improving the biocidal activity.

From these considerations, it is possible to analyze how the excited electron located in the CB can reduce the adsorbed O_2 molecule to generate $^{\bullet}O_2^-$. To this end, an additional electron was considered as a free charge along the exposed surface, and the spin density distribution was analyzed to disclose the charge transfer mechanism between the SiO_2 surface and the O_2 molecule. The results are displayed in Figure 5.

An analysis of the results displays that models A and C exhibit the largest charge electron transfer from the surface to the adsorbed O_2, with a concomitant increase of O−O bond length, while the Ag−O_2 bond length is reduced. In this case, the excess of electrons can be depicted by the contours of the spin-down isosurface along the *yz*-plane. The adsorbed O_2 molecule is favorable for the production of $^{\bullet}O_2^-$ through an electron transfer process. On the other hand, in the model B, there is a large spin density distribution along the Ag_4 cluster, resulting in a shrinkage of the O_2 bond length. Therefore, first, O_2 can be easily adsorbed on the surface of pristine and defective SiO_2−Ag systems due to their higher adsorption energy. Second, there is an electron transfer process from the CB to adsorbed O_2, as the starting step for the formation of $^{\bullet}O_2^-$.

Mulliken atomic charges were calculated, and the charger transfer from the SiO_2−Ag models to adsorbed O_2 was calculated to be −0.73 (A), −0.63 (B), and −0.71 lel (C). These values are a signature de the posterior formation of $^{\bullet}O_2^-$. On the other hand, there is a shortening of the distance between the $^{\bullet}O_2^-$ and the neighboring H atoms, indicating that a further reaction step along such a surface can induce the formation of $^{\bullet}O_2H$. The proton transfer mechanism was considered for the pristine SiO_2−Ag model due to the proximity between the super anion radical ($^{\bullet}O_2^-$) and the neighboring Si−OH groups, as depicted in Figure 6.

Indeed, the $^{\bullet}HO_2$ radical can be visualized by the short O_2−H bond distance resulting from the capture of H^+ from the neighboring Si−OH, which directly interacts with the Ag_4 cluster through a new Ag−O chemical bond.

3.2.3. H_2O Adsorption Process and ROS Generation Mechanism. The values of adsorption energy and the corresponding optimized geometries of the adsorption process of H_2O in models A, B, and C are presented in Figure 7.

In this case, it was noted that the H_2O molecule adsorbs on the SiO_2 surface following the order B > C > A. Indeed, for the defective SiO_2−Ag models, the adsorption mechanism seems to be a chemisorption due to the formation of Ag−O and O−

https://doi.org/10.1021/acsami.2c21011
ACS Appl. Mater. Interfaces 2023, 15, 6548−6560

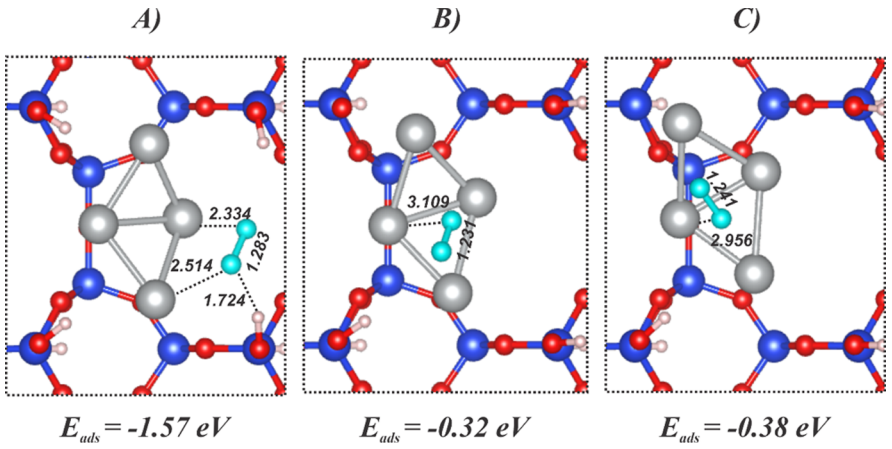

Figure 4. Top views of O_2 adsorption (cyan) on the A, B, and C models. Selected values of O−O, Ag−O, and H−O distances (Å) and values of adsorption energies (E_{ads}) were included for comparison purposes.

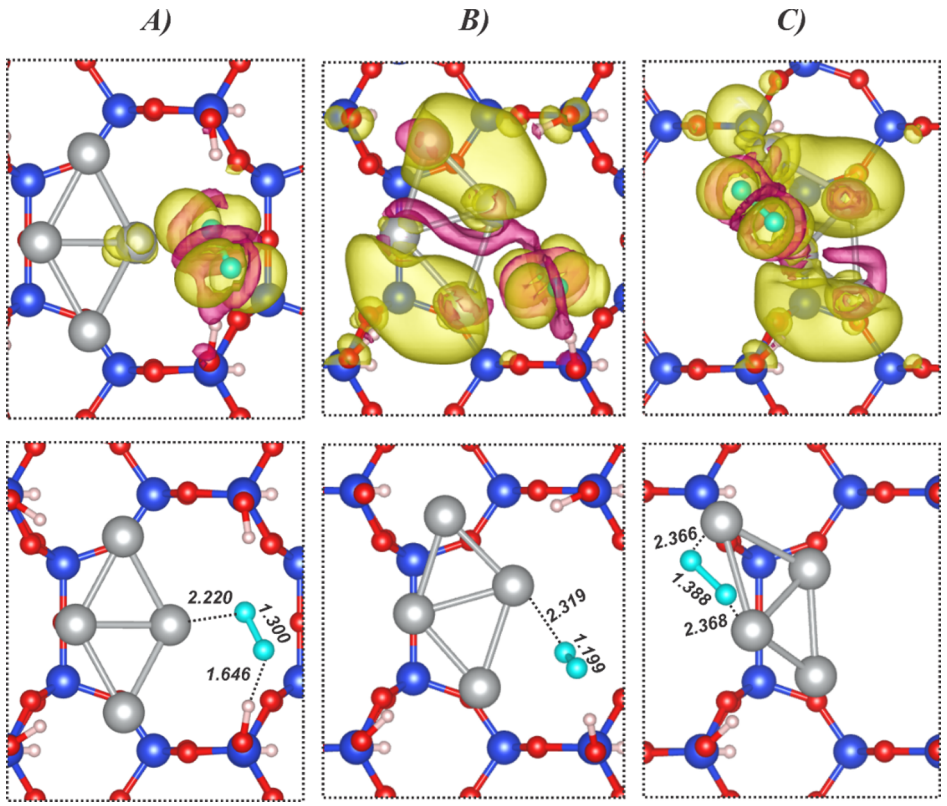

Figure 5. Spin density isosurfaces (0.001 e/Å^3) for the O_2 adsorption process (cyan) on A, B, and C models after the addition of an electron. Yellow and magenta isosurfaces represent spin-up and spin-down densities, respectively.

H bonding paths with reduced bond length in comparison with the pristine model. This fact can be associated with the reactivity of paramagnetic defects along the exposed surface of SiOH−Ag since the adsorbed H_2O molecules are located in the vicinity of both defects, with concomitant interaction of both the Ag_4 cluster and the $[SiO_4{\cdots}V_H]$ and $[SiO_3{\cdots}V_{OH}]$ centers.

Figure 8 depicts the spin density distribution for all models, showing the electron transfer between the adsorbed H_2O molecule and the superficial Ag_4, $[SiO_4{\cdots}V_H]$, and $[SiO_3{\cdots}V_{OH}]$ clusters. In particular, the spin density localization caused by the adsorbed H_2O molecules results in a shrinkage of Ag−OH_2 bond interactions and an increase in some O−H bonds, in agreement with the donation of electrons between the adsorbed species and the surface layer. An interesting point can be observed for the naturally defective systems B and C: their higher adsorption enthalpy follows the increased density distribution involving Ag_4, $[SiO_4{\cdots}V_H]$, and $[SiO_3{\cdots}V_{OH}]$ centers.

In addition, SiO_2−Ag model B exhibits a very interesting mechanism after charge transfer from the adsorbed H_2O molecule, when one of the O−H bonds becomes larger due to the interaction with neighboring defects. This fact agrees with the hypothesis that after hole scavenging the H_2O molecule can release one H^+ and form the hydroxyl radical species ($^{\bullet}OH$). Therefore, a proton transfer from adsorbed H_2O to defective $[SiO_4{\cdots}V_H]$ centers can take place, as presented in Figure 9. In this case, it was observed that after the proton

https://doi.org/10.1021/acsami.2c21011
ACS Appl. Mater. Interfaces 2023, 15, 6548−6560

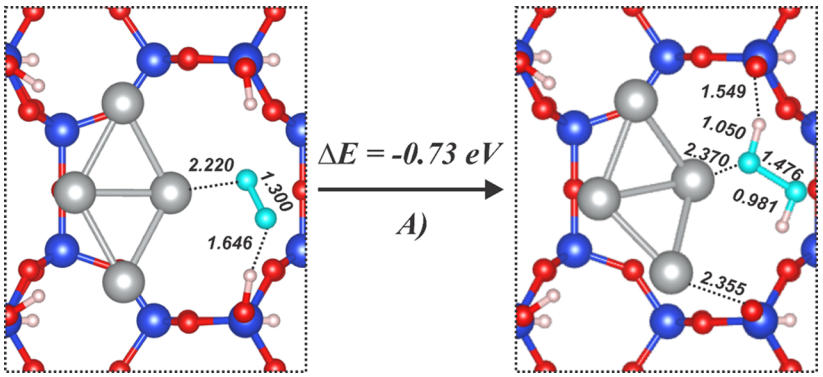

Figure 6. Optimized geometries of the O_2 (in cyan) adsorbed in model A before (left panel) and after (right panel) proton transfer.

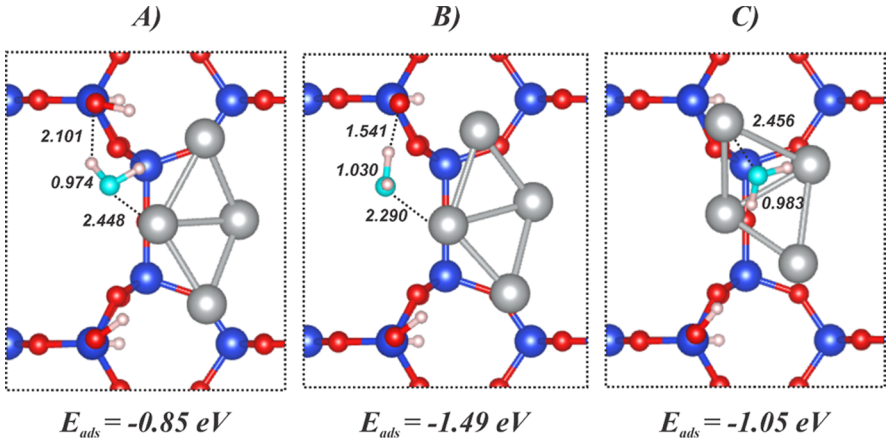

Figure 7. Top views of H_2O adsorption (cyan) on A, B, and C models. Selected values of O−O, Ag−O, and H−O distances (Å) and the values of adsorption energies (E_{ads}) were included for comparison purposes.

transfer process from the adsorbed H_2O molecule, the $[SiO_4 \cdots V_H]$ becomes a superficial Si−OH group, while the remaining hydroxyl radical species ($^{\bullet}OH$) is adsorbed on the Ag_4 cluster, changing its symmetry for a tetrahedral environment.

3.3. On the Mechanisms of Biocidal Activity. The molecular mechanism by which nanostructures eliminate pathogens has not been thoroughly investigated and remains unclear. For this reason, the formation of ROS on the semiconductor surfaces has been a topic of tremendous scientific interest because of their essential role in photocatalytic and biological processes. Thus, understanding the production and distribution of ROS on the semiconductor photocatalyst surface is crucial not only to clarify the photocatalysis and biocidal activity mechanisms but also to improve the efficiency of chemical reactions.[62−64] It is worth mentioning that ROS are also responsible for the biocidal activity of semiconductor surfaces due to their ability to kill pathogens directly by oxidative damage to biological compounds or indirectly by nonoxidative pathways such as autophagy or T-lymphocyte responses.[64−67]

The nanoparticles that induce oxidative stress could be used to boost the antimicrobial (antibacterial and antiviral) activities based on the control of physicochemical properties in order to direct the oxidative stress toward specific targets, for example, the elimination of the SARS-CoV-2 virus. In this context, the consideration of SiO_2 as a matrix for the functionalization of nanoparticles is very important since the silica particles have the ability to attach themselves to enveloped viruses via hydrophobic/hydrophilic interactions through the different moieties along the exposed surface.[68−70] Moreover, the SiO_2 matrix can be mixed with different metals to reduce its band gap energy, inducing a p/n-type semiconductor behavior that depends on the electronic structure of the metal and contributing to a photoinduced antimicrobial activity.[71]

Herein, the combination of hydroxylated SiO_2 surfaces and Ag nanoparticles was investigated to understand the process involved in the remarkable biocidal activity of SiO_2−Ag nanoparticles. Based on the above results, it is possible to argue that the hydroxyl radical species ($^{\bullet}OH$) and the hydrogen peroxide radical ($^{\bullet}HO_2$) can be generated from H_2O and O_2 adsorption on the Ag-decorated SiO_2 surfaces. After the O_2 adsorption and reduction processes provoked by the excited electrons at the CB of SiO_2−Ag, the possibility to generate the hydrogen peroxide radical ($^{\bullet}HO_2$) is favored even with the deprotonation of superficial Si−OH species. On the other hand, the H_2O adsorption mechanism involves a smaller charge transfer, which indicates that photogenerated holes are only partially trapped by the electron donation, causing them to exhibit an important activity due to their location in Ag clusters.

It was also confirmed that common defects present on the SiO_2 surfaces are essential to increase H_2O adsorption and dissociation, while the oxygen-mediated process seems to be favorable to pristine SiO_2−Ag surfaces. These defects can even enhance the photogeneration of charge carriers due to the band gap narrowing that efficiently increases the electron flow along the SiOH−Ag interaction and facilitates the charge separation.

https://doi.org/10.1021/acsami.2c21011
ACS Appl. Mater. Interfaces 2023, 15, 6548−6560

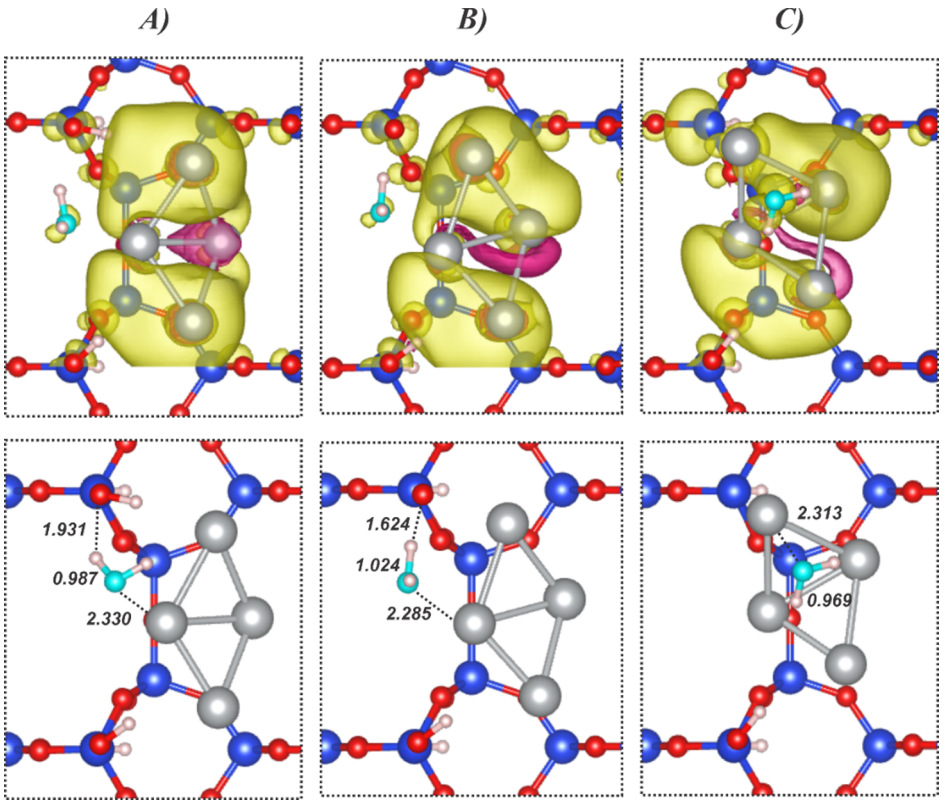

Figure 8. Spin density isosurfaces (0.001 e/Å^3) for the H_2O (in cyan) adsorption process on A, B, and C models after interaction with the electron-deficient model (hole).

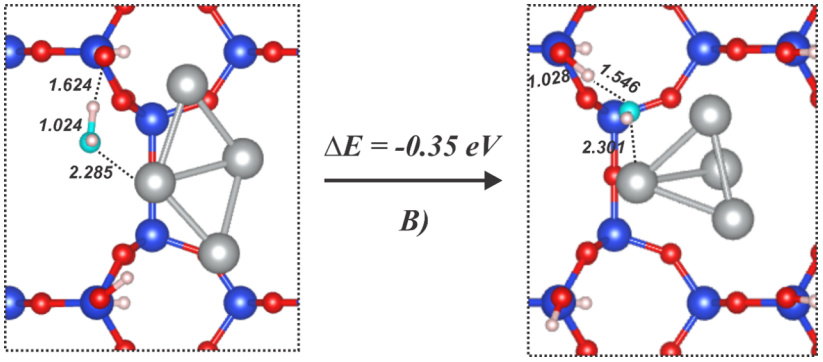

Figure 9. Optimized geometries of the H_2O (in cyan) adsorption process in model B before (left panel) and after (right panel) proton transfer. The blue, gray, and red balls represent the Si, Ag, and O atoms, respectively.

Furthermore, it was proved that the O_2 adsorption mechanism on pristine SiO_2−Ag surfaces induces the formation of defects through the deprotonation of superficial Si−OH species to generate the hydrogen peroxide radical ($^{\bullet}HO_2$). However, SiO_2−Ag model B indicates that after hole trapping by adsorbed H_2O molecules the defective Si−O site captures a proton from H_2O, restoring the hydroxylated silica surfaces, while the remaining hydroxyl radical species ($^{\bullet}OH$) is adsorbed on the Ag_4 cluster. This shows that the interaction between O_2/H_2O and SiO_2−Ag surfaces is responsible for ROS generation, evidencing the great importance of the electronic features of silver-decorated surfaces.

As a summary, a general mechanism can be proposed using the Kroger−Vink notation,[72] and a schematic representation is presented in Figure 10. In this formalism, the charge accumulation mechanism could be described using the neutral $[MO_n/M]^x$, positively charged $V_O^{\bullet}$, and negatively charged $[MO_n/M]'$ clusters. The SiO_2 framework is composed of the moieties $[SiO_2]_A$, while the nanoparticles of Ag are represented by $[Ag]_c$. SiO_2 as a semiconductor can be seen as a dynamic system that works as a quantum cluster, able to act as both a donor and receptor of electrons. These clusters on the surface may have different absorption or reception capacity of electrons, depending on the type of structural defects (distorted bond distances, Si−O, and angles, O−Si−O) and the electron distribution in the short, medium, and long ranges. Thus, the quantum clusters can be classified as organized or disorganized structures randomly distributed on the crystal surface in the ground or excited electronic states. Therefore, there are cluster-to-cluster charge transfer processes related to each kind of cluster, which are characterized by excitations

https://doi.org/10.1021/acsami.2c21011
ACS Appl. Mater. Interfaces 2023, 15, 6548−6560

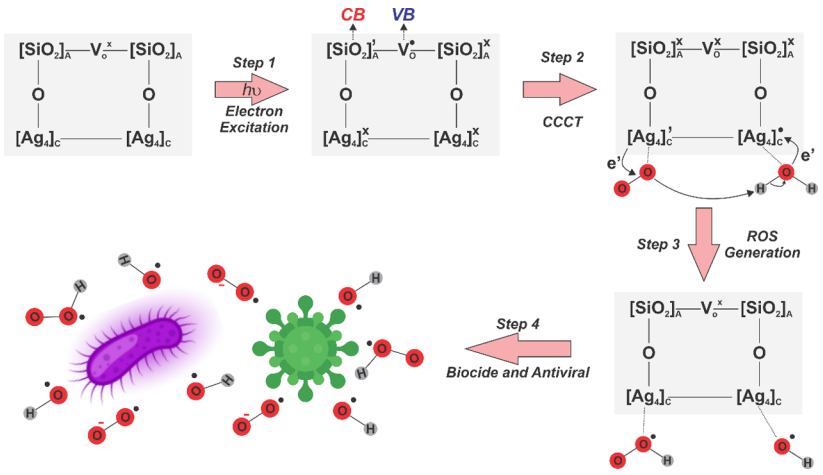

Figure 10. Schematic representation of the steps involved in the ROS generation on SiO_2−Ag surfaces. $[SiO_2]_A$ and $[Ag_4]_c$ correspond to asymmetric SiO_2 and symmetric Ag_4 moieties, respectively, while VB and CB represent valence and conduction bands, respectively.

involving electronic transitions among neighboring SiO_4 clusters, maintaining the electron density.

In previous experimental investigations[28,29] it was observed that hole (h^+), hydroxyl radical ($^{\bullet}OH$), and hydroperoxyl radical ($^{\bullet}HO_2$) are the reactive species along the mechanism of the biocidal activity of SiO_2−Ag composite. Herein, the formation of ROS can be rationalized by the active participation of oxygen, O_2, and water, H_2O, molecules. The cluster with the highest electron density transfers an electron, e′, from the CB to O_2, to generate the superoxide anion radical, $^{\bullet}O_2^-$. Simultaneously, there is a decrease in the electron density near the VB, associated with the oxygen vacancy, of the adjacent $[SiO_4]$ cluster. This electronic imbalance facilitates the decomposition of H_2O after the interaction with the hole located at the VB, donating one electron to the SiO_2−Ag surface that generates a hydroxyl radical, $^{\bullet}OH$, and a proton, H^+, which can react with $^{\bullet}O_2^-$, to form the hydroperoxyl radical, $^{\bullet}HO_2$. These ROS can generate new highly oxidizing species (i.e., singlet oxygen, $^1O_2$, or/and hydrogen peroxide, H_2O_2), which enhance the biocidal activity of the material.

Based on the above mechanism, the SiO_2−Ag composite incorporated into different polymeric matrix stands out as an exciting biocidal material that can be used as coating technologies that prevent the microbial contamination, especially for the SARS-CoV-2 virus, contributing to the fight against the COVID-19 commonly transmitted by air[73] through the development of antiviral face masks as well as to combat the viral spreading in solid/plastic environments by using advanced coating surface.[74]

4. CONCLUSIONS

The SARS-CoV-2 pandemic has shed light on the importance of investigating different materials to deal with global health problems associated with microorganism infections. Facile and economical process, which is also eco-friendly involving the synthesis and development of innovative materials able to prevent not only the transmission, spread, and entry of virus) but also bacteria and fungi into the human body is in the spotlight. It is known that SiO_2−Ag composites reveal unique electronic and magnetic properties, which are responsible for their enhanced biocidal activity. To disentangle this activity, associated to the quantum confinement effect on the metal/oxide interfaces, here, a joint experimental and theoretical study is carried out.

The main conclusions of the present work can be summarized as follows: (i) we performed DFT calculations and a variety of experimental techniques to disclose the enhanced biocidal activity of the SiO_2−Ag composite in the LDPE; (ii) the biological assays showed that the SiO_2−Ag composite can eliminate *S. aureus* and SARS-CoV-2, with the latter being almost entirely eliminated (99.99%) in just 2 min; (iii) after analyzing the DFT−DOS, the presence of Ag components provokes a decrease of bandgap energy for SiO_2−Ag_4 cluster, which can be associated to the good biocidal behavior; (iv) DFT results explain how electron would be scavenged by O_2 in H_2O to produce ROS ($^{\bullet}O_2^-$, $^{\bullet}OH$, and $^{\bullet}HO_2$). More realistic simulations including H_2O and O_2 environments, such as molecular dynamics with appropriate potentials, will be the basis of future work; (v) these findings offer a new perspective of energy and charge transfer processes on the adsorption of both O_2 and H_2O molecules on the pristine and defective hydroxylated SiO_2 surfaces decorated with Ag_4 clusters; (vi) to the best of our knowledge, this is the first direct evidence of how structural and electronic features of SiO_2 with Ag nanoparticles may explain the enhanced activity of the SiO_2−Ag composite as a biocidal material, especially in the fight against COVID-19; and (vii) our study might open new avenues for designing new materials by means of surface engineering that can be applicable to a wide range of metal nanoparticles/semiconductors. We anticipate that the demand for novel biocidal technologies will grow exponentially as countries prepare themselves for a post-COVID-19 world in which new pandemics will appear. These new technologies will include long-lasting efficacies without reapplication, fast killing kinetics, low environmental burden, and a minimized the presence multi drug-resistant pathogens.

■ ASSOCIATED CONTENT

Supporting Information

The Supporting Information is available free of charge at https://pubs.acs.org/doi/10.1021/acsami.2c21011.

Schematic representations of computational models used to build the SiO_2−Ag composite describing the SiO_2 amorphous representation, superficial silanol groups, vacancies, and Ag_4 cluster; representations of

https://doi.org/10.1021/acsami.2c21011
ACS Appl. Mater. Interfaces 2023, 15, 6548−6560

SiO_2−Ag optimized models; and DOSs for SiO_2 and SiO_2−Ag models (PDF)

AUTHOR INFORMATION

Corresponding Author

Marisa Carvalho de Oliveira − *Functional Materials Development Center (CDMF), Federal University of São Carlos—UFSCar, 13565-905 São Carlos, São Paulo, Brazil;* orcid.org/0000-0003-3392-7489; Email: marisacoliveira31@gmail.com

Authors

Marcelo Assis − *Department of Physical and Analytical Chemistry, University Jaume I—UJI, 12071 Castelló de la Plana, Spain;* orcid.org/0000-0003-0355-5565

Luiz Gustavo Pagotto Simões − *Nanox Tecnologia S/A, 13562-400 São Carlos, São Paulo, Brazil*

Daniel Tamassia Minozzi − *Nanox Tecnologia S/A, 13562-400 São Carlos, São Paulo, Brazil*

Renan A. P. Ribeiro − *Department of Natural Science, Minas Gerais State University—UEMG, 35501-170 Divinópolis, Minas Gerais, Brazil;* orcid.org/0000-0002-4128-8296

Juan Andrés − *Department of Physical and Analytical Chemistry, University Jaume I—UJI, 12071 Castelló de la Plana, Spain;* orcid.org/0000-0003-0232-3957

Elson Longo − *Functional Materials Development Center (CDMF), Federal University of São Carlos—UFSCar, 13565-905 São Carlos, São Paulo, Brazil;* orcid.org/0000-0001-8062-7791

Complete contact information is available at: https://pubs.acs.org/10.1021/acsami.2c21011

Notes

The authors declare no competing financial interest.

ACKNOWLEDGMENTS

The authors would like to thank the following research funding agencies for their financial support: CNPQ, CAPES, FAPESP (2013/07296-2 and 2021/01651-1), FAPEMIG (APQ-00079-21), UEMG for the Productivity Program, Universitat Jaume I (project UJI-B2019-30), Ministerio de Ciencia, Innovación y Universidades (Spain) (project PGC2018094417-B-I00) and Margarita Salas postdoctoral contract MGS/2021/21 (UP2021-021) financed by the European Union-NextGenerationEU. The authors are also grateful to the National Laboratory for Scientific Computing (LNCC) and the High-Performance Computing Center (NACAD) at COPPE-UFRJ and to the National Center for High-Performance Computing (CENAPAD) at UNICAMP and UFMG for providing computing resources.

REFERENCES

(1) Steffan, J. J.; Derby, J. A.; Brevik, E. C. Soil Pathogens that may Potentially Cause Pandemics, Including Severe Acute Respiratory Syndrome (SARS) Coronaviruses. *Curr. Opin. Environ. Sci. Health* **2020**, *17*, 35−40.

(2) Dev Kumar, G.; Mishra, A.; Dunn, L.; Townsend, A.; Oguadinma, I. C.; Bright, K. R.; Gerba, C. P. Biocides and Novel Antimicrobial Agents for the Mitigation of Coronaviruses. *Front. Microbiol.* **2020**, *11*, 1351.

(3) Behzadinasab, S.; Chin, A.; Hosseini, M.; Poon, L.; Ducker, W. A. A Surface Coating that Rapidly Inactivates SARS-CoV-2. *ACS Appl. Mater. Interfaces* **2020**, *12*, 34723−34727.

(4) Kiremitler, N. B.; Kemerli, M. Z.; Kayaci, N.; Karagoz, S.; Pekdemir, S.; Sarp, G.; Sanduvac, S.; Onses, M. S.; Yilmaz, E. Nanostructures for the Prevention, Diagnosis, and Treatment of SARS-CoV-2: A Review. *ACS Appl. Nano Mater.* **2022**, *5*, 6029−6054.

(5) Shaw, Z. L.; Kuriakose, S.; Cheeseman, S.; Dickey, M. D.; Genzer, J.; Christofferson, A. J.; Crawford, R. J.; McConville, C. F.; Chapman, J.; Truong, V. K.; Elbourne, A.; Walia, S. Antipathogenic Properties and Applications of Low-Dimensional Materials. *Nat. Commun.* **2021**, *12*, 3897.

(6) Larrañaga-Altuna, M.; Zabala, A.; Llavori, I.; Pearce, O.; Nguyen, D. T.; Caro, J.; Mescheder, H.; Endrino, J. L.; Goel, G.; Ayre, W. N.; Seenivasagam, R. K.; Tripathy, D. K.; Armstrong, J.; Goel, S. Bactericidal Surfaces: An Emerging 21st-Century Ultra-Precision Manufacturing and Materials Puzzle. *Appl. Phys. Rev.* **2021**, *8*, 021303.

(7) Riduan, S. N.; Zhang, Y. Recent Advances of Zinc-based Antimicrobial Materials. *Chem.—Asian J.* **2021**, *16*, 2588−2595.

(8) Quek, J. Y.; Uroro, E.; Goswami, N.; Vasilev, K. Design Principles for Bacteria-Responsive Antimicrobial Nanomaterials. *Mater. Today Chem.* **2022**, *23*, 100606.

(9) Valenzuela, L.; Iglesias-Juez, A.; Bachiller-Baeza, B.; Faraldos, M.; Bahamonde, A.; Rosal, R. Biocide Mechanism of Highly Efficient and Stable Antimicrobial Surfaces Based on Zinc Oxide−Reduced Graphene Oxide Photocatalytic Coatings. *J. Mater. Chem. B* **2020**, *8*, 8294−8304.

(10) Abebe, B.; Zereffa, E. A.; Tadesse, A.; Murthy, H. C. A. A Review on Enhancing the Antibacterial Activity of ZnO: Mechanisms and Microscopic Investigation. *Nanoscale Res. Lett.* **2020**, *15*, 190.

(11) Gudkov, S. V.; Burmistrov, D. E.; Serov, D. A.; Rebezov, M. B.; Semenova, A. A.; Lisitsyn, A. B. Do Iron Oxide Nanoparticles Have Significant Antibacterial Properties? *Antibiotics* **2021**, *10*, 884.

(12) Riduan, S. N.; Zhang, Y. Nanostructured Surfaces with Multimodal Antimicrobial Action. *Acc. Chem. Res.* **2021**, *54*, 4508−4517.

(13) Nosaka, Y.; Nosaka, A. Y. Generation and Detection of Reactive Oxygen Species in Photocatalysis. *Chem. Rev.* **2017**, *117*, 11302−11336.

(14) Corma, A.; Botella, P.; Rivero-Buceta, E. Silica-Based Stimuli-Responsive Systems for Antitumor Drug Delivery and Controlled Release. *Pharmaceutics* **2022**, *14*, 110.

(15) Lin, Y.-H.; Chen, Y.-P.; Liu, T.-P.; Chien, F.-C.; Chou, C.-M.; Chen, C.-T.; Mou, C.-Y. Approach To Deliver Two Antioxidant Enzymes with Mesoporous Silica Nanoparticles into Cells. *ACS Appl. Mater. Interfaces* **2016**, *8*, 17944−17954.

(16) Chen, Y.-P.; Chen, C.-T.; Hung, Y.; Chou, C.-M.; Liu, T.-P.; Liang, M.-R.; Chen, C.-T.; Mou, C.-Y. A New Strategy for Intracellular Delivery of Enzyme Using Mesoporous Silica Nanoparticles: Superoxide Dismutase. *J. Am. Chem. Soc.* **2013**, *135*, 1516−1523.

(17) Wu, S.-H.; Mou, C.-Y.; Lin, H.-P. Synthesis of Mesoporous Silica Nanoparticles. *Chem. Soc. Rev.* **2013**, *42*, 3862−3875.

(18) Scheffer, F. R.; Silveira, C. P.; Morais, J.; Bettini, J.; Cardoso, M. B. Tailoring Pseudo-Zwitterionic Bifunctionalized Silica Nanoparticles: From Colloidal Stability to Biological Interactions. *Langmuir* **2020**, *36*, 10756−10763.

(19) de Souza e Silva, J. M.; Hanchuk, T. D. M.; Santos, M. I.; Kobarg, J.; Bajgelman, M. C.; Cardoso, M. B. Viral Inhibition Mechanism Mediated by Surface-Modified Silica Nanoparticles. *ACS Appl. Mater. Interfaces* **2016**, *8*, 16564−16572.

(20) Macchione, M. A.; Biglione, C.; Strumia, M. Design, Synthesis and Architectures of Hybrid Nanomaterials for Therapy and Diagnosis Applications. *Polymers* **2018**, *10*, 527.

(21) Paternò, G. M.; Ross, A. M.; Pietralunga, S. M.; Normani, S.; Dalla Vedova, N.; Limwongyut, J.; Bondelli, G.; Moscardi, L.; Bazan, G. C.; Scotognella, F.; Lanzani, G. The Impact of Bacteria Exposure on the Plasmonic Response of Silver Nanostructured Surfaces. *Chem. Phys. Rev.* **2021**, *2*, 021401.

(22) Urnukhsaikhan, E.; Bold, B.-E.; Gunbileg, A.; Sukhbaatar, N.; Mishig-Ochir, T. Antibacterial Activity and Characteristics of Silver

Nanoparticles Biosynthesized from Carduus Crispus. *Sci. Rep.* **2021**, *11*, 21047.
(23) Jeremiah, S. S.; Miyakawa, K.; Morita, T.; Yamaoka, Y.; Ryo, A. Potent Antiviral Effect of Silver Nanoparticles on SARS-CoV-2. *Biochem. Biophys. Res. Commun.* **2020**, *533*, 195−200.
(24) Wang, X.; Wang, Y.; Li, X.; Du, X. Mesoporous Silica Nanosheets with Well-Dispersed Small Ag Nanoparticles for the Construction of Robust Transparent Antibacterial Nanocoatings. *Microporous Mesoporous Mater.* **2021**, *328*, 111476.
(25) Vallet-Regí, M.; Schüth, F.; Lozano, D.; Colilla, M.; Manzano, M. Engineering Mesoporous Silica Nanoparticles For Drug Delivery: Where Are We After Two Decades? *Chem. Soc. Rev.* **2022**, *51*, 5365−5451.
(26) Affonso de Oliveira, J. F.; Scheffer, F. R.; Landis, R. F.; Teixeira Neto, É.; Rotello, V. M.; Cardoso, M. B. Dual Functionalization of Nanoparticles for Generating Corona-Free and Noncytotoxic Silica Nanoparticles. *ACS Appl. Mater. Interfaces* **2018**, *10*, 41917−41923.
(27) Vanichvattanadecha, C.; Singhapong, W.; Jaroenworaluck, A. Different Sources of Silicon Precursors Influencing on Surface Characteristics and Pore Morphologies of Mesoporous Silica Nanoparticles. *Appl. Surf. Sci.* **2020**, *513*, 145568.
(28) Assis, M.; Simoes, L. G. P.; Tremiliosi, G. C.; Coelho, D.; Minozzi, D. T.; Santos, R. I.; Vilela, D. C. B.; Santos, J. R. d.; Ribeiro, L. K.; Rosa, I. L. V.; Mascaro, L. H.; Andrés, J.; Longo, E. SiO_2-Ag Composite as a Highly Virucidal Material: A Roadmap that Rapidly Eliminates SARS-CoV-2. *Nanomaterials* **2021**, *11*, 638.
(29) Assis, M.; Simoes, L. G. P.; Tremiliosi, G. C.; Ribeiro, L. K.; Coelho, D.; Minozzi, D. T.; Santos, R. I.; Vilela, D. C. B.; Mascaro, L. H.; Andrés, J.; Longo, E. PVC-SiO_2-Ag Composite as a Powerful Biocide and Anti-SARS-CoV-2 Material. *J. Polym. Res.* **2021**, *28*, 361.
(30) Hosseini, M.; Chin, A. W. H.; Williams, M. D.; Behzadinasab, S.; Falkinham, J. O., III; Poon, L. L. M.; Ducker, W. A. Transparent Anti-SARS-CoV-2 and Antibacterial Silver Oxide Coatings. *ACS Appl. Mater. Interfaces* **2022**, *14*, 8718−8727.
(31) Kumar Sen, S.; Raut, S. Microbial Degradation of Low Density Polyethylene (LDPE): A Review. *J. Environ. Chem. Eng.* **2015**, *3*, 462−473.
(32) Basmage, O. M.; Hashmi, M. S. J.Plastic Products in Hospitals and Healthcare Systems. In *Encyclopedia of Renewable and Sustainable Materials*; Hashmi, S., Choudhury, I. A., Eds.; Elsevier: Oxford, 2020; pp 648−657.
(33) Organization, I. S.*Measurement of Antiviral Activity on Plastics and Other Non-porous Surfaces*; International Standardization Organization: Geneva, Switzerland, 2017. 21702.
(34) Organization, I. S.*Measurement of Antiviral Activity on Plastics and Other Non-porous Surfaces*; International Standardization Organization: Geneva, Switzerland, 2019. 21702:2019.
(35) Miller, J.; Ulrich, R. On the Analysis of Psychometric Functions: The Spearman-Kärber Method. *Percept. Psychophys.* **2001**, *63*, 1399−1420.
(36) Reed, L. J.; Muench, H. A Simple Method of Estimating Fifty per Cent Endpoints 12. *Am. J. Epidemiol.* **1938**, *27*, 493−497.
(37) Organization, I. S.*2013 Plastics—Methods of Exposure to Laboratory Light Sources—Part 2: Xenon-Arc Lamps*; International Standardization Organization: Geneva, Switzerland, 2013. 4892-2.
(38) Grimme, S.; Antony, J.; Ehrlich, S.; Krieg, H. A Consistent and Accurate Ab Initio Parametrization of Density Functional Dispersion Correction (DFT-D) for the 94 Elements H-Pu. *J. Chem. Phys.* **2010**, *132*, 154104.
(39) Dovesi, R.; Erba, A.; Orlando, R.; Zicovich-Wilson, C. M.; Civalleri, B.; Maschio, L.; Rérat, M.; Casassa, S.; Baima, J.; Salustro, S.; Kirtman, B. Quantum-Mechanical Condensed Matter Simulations with CRYSTAL. *Wiley Interdiscip. Rev.: Comput. Mol. Sci.* **2018**, *8*, No. e1360.
(40) Tosoni, S.; Civalleri, B.; Pascale, F.; Ugliengo, P. Hydroxylated Crystalline Edingtonite Silica Faces as Models for the Amorphous Silica Surface. *J. Phys.: Conf. Ser.* **2008**, *117*, 012026.
(41) Aprà, E.; Stefanovich, E.; Dovesi, R.; Roetti, C. An Ab Initio Hartree-Fock Study of Silver Chloride. *Chem. Phys. Lett.* **1991**, *186*, 329−335.
(42) Gierada, M.; De Proft, F.; Sulpizi, M.; Tielens, F. Understanding the Acidic Properties of the Amorphous Hydroxylated Silica Surface. *J. Phys. Chem. C* **2019**, *123*, 17343−17352.
(43) Tielens, F.; Gierada, M.; Handzlik, J.; Calatayud, M. Characterization of Amorphous Silica Based Catalysts using DFT Computational Methods. *Catal. Today* **2020**, *354*, 3−18.
(44) Tielens, F.Characterization of Amorphous Silica-Based Materials Using DFT Computational Methods. In *Chemistry of Silica and Zeolite-Based Materials*; Douhal, A., Anpo, M., Eds.; Elsevier, 2019; Vol. 2, pp 351−374.
(45) Deraet, X.; Turek, J.; Alonso, M.; Tielens, F.; Cottenier, S.; Ayers, P. W.; Weckhuysen, B. M.; De Proft, F. Reactivity of Single Transition Metal Atoms on a Hydroxylated Amorphous Silica Surface: A Periodic Conceptual DFT Investigation. *Chem.—Eur. J.* **2021**, *27*, 6050−6063.
(46) Berro, Y.; Badawi, M.; El Haj Hassan, F.; Kassir, M.; Tielens, F. Water-Silanol Interactions on the Amorphous Silica Surface: A Dispersion-Corrected DFT Investigation. *J. Mol. Liq.* **2020**, *320*, 114496.
(47) Sulimov, A. V.; Kutov, D. C.; Grigoriev, F. V.; Tikhonravov, A. V.; Sulimov, V. B. Generation of Amorphous Silicon Dioxide Structures via Melting-Quenching Density Functional Modeling. *Lobachevskii J. Math.* **2020**, *41*, 1581−1590.
(48) Rimola, A.; Costa, D.; Sodupe, M.; Lambert, J.-F.; Ugliengo, P. Silica Surface Features and Their Role in the Adsorption of Biomolecules: Computational Modeling and Experiments. *Chem. Rev.* **2013**, *113*, 4216−4313.
(49) Delle Piane, M.; Corno, M.; Ugliengo, P.Ab Initio Modeling of Hydrogen Bond Interaction at Silica Surfaces With Focus on Silica/Drugs Systems. In *Modelling and Simulation in the Science of Micro- and Meso-Porous Materials*; Catlow, C. R. A., Van Speybroeck, V., van Santen, R. A., Eds.; Elsevier, 2018; pp 297−328.
(50) Ugliengo, P.; Sodupe, M.; Musso, F.; Bush, I. J.; Orlando, R.; Dovesi, R. Realistic Models of Hydroxylated Amorphous Silica Surfaces and MCM-41 Mesoporous Material Simulated by Large-scale Periodic B3LYP Calculations. *Adv. Mater.* **2008**, *20*, 4579−4583.
(51) Musso, F.; Ugliengo, P.; Solans-Monfort, X.; Sodupe, M. Periodic DFT Study of Radical Species on Crystalline Silica Surfaces. *J. Phys. Chem. C* **2010**, *114*, 16430−16438.
(52) Civalleri, B.; Ugliengo, P. First Principles Calculations of the Adsorption of NH3 on a Periodic Model of the Silica Surface. *J. Phys. Chem. B* **2000**, *104*, 9491−9499.
(53) Civalleri, B.; Casassa, S.; Garrone, E.; Pisani, C.; Ugliengo, P. Quantum Mechanical ab Initio Characterization of a Simple Periodic Model of the Silica Surface. *J. Phys. Chem. B* **1999**, *103*, 2165−2171.
(54) Chen, D.; Zhang, X.; Tang, J.; Cui, H.; Li, Y.; Zhang, G.; Yang, J. Density functional theory study of small Ag cluster adsorbed on graphyne. *Appl. Surf. Sci.* **2019**, *465*, 93−102.
(55) Benabid, F.; Kharchi, N.; Zouai, F.; Mourad, A.-H. I.; Benachour, D. Impact of Co-Mixing Technique and Surface Modification of ZnO Nanoparticles Using Stearic Acid on their Dispersion into HDPE to Produce HDPE/ZnO Nanocomposites. *Polym. Polym. Compos.* **2019**, *27*, 389−399.
(56) Papajanı, B.; Sınanaj, A.; Hasımı, A. V.; Vataj, E. The Study of the Influence of Additives in the Crystallinity of Recycled Ldpe by Ir and Xrd Analysis. *RAD Conf. Proc.* **2018**, *3*, 236−240.
(57) Zweiback, J.; Ditmire, T.; Perry, M. D. Resonance in Scattering and Absorption from Large Noble Gas Clusters. *Opt. Express* **2000**, *6*, 236−242.
(58) Wang, J.; Mbah, C. F.; Przybilla, T.; Apeleo Zubiri, B.; Spiecker, E.; Engel, M.; Vogel, N. Magic Number Colloidal Clusters as Minimum Free Energy Structures. *Nat. Commun.* **2018**, *9*, 5259.
(59) Huerta-Aguilar, C. A.; Diaz-Puerto, Z. J.; Tecuapa-Flores, E. D.; Thangarasu, P. Crystal Plane Impact of $ZnFe_2O_4$−Ag Nanoparticles Influencing Photocatalytical and Antibacterial Properties: Experimental and Theoretical Studies. *ACS Omega* **2022**, *7*, 33985−34001.

https://doi.org/10.1021/acsami.2c21011
ACS Appl. Mater. Interfaces 2023, 15, 6548−6560

(60) Jiang, D.; Wang, W.Chapter 11—Fundamental Studies on Photocatalytic Structures With Well-Defined Crystal Facets. *Studies in Surface Science and Catalysis*; Fornasiero, P., Cargnello, M., Eds.; Elsevier, 2017; Vol. *177*, pp 409−438.
(61) Gouveia, A. F.; Gracia, L.; Longo, E.; San-Miguel, M. A.; Andrés, J. Modulating the Properties of Multifunctional Semiconductors by Means of Morphology: Theory Meets Experiments. *Comput. Mater. Sci.* **2021**, *188*, 110217.
(62) Zhang, C.; Wang, X.; Du, J.; Gu, Z.; Zhao, Y. Reactive Oxygen Species-Regulating Strategies Based on Nanomaterials for Disease Treatment. *Adv. Sci.* **2021**, *8*, 2002797.
(63) Zhang, L.; Zhu, C.; Huang, R.; Ding, Y.; Ruan, C.; Shen, X.-C. Mechanisms of Reactive Oxygen Species Generated by Inorganic Nanomaterials for Cancer Therapeutics. *Front. Chem.* **2021**, *9*, 630969.
(64) Sander, W. J.; Fourie, C.; Sabiu, S.; O'Neill, F. H.; Pohl, C. H.; O'Neill, H. G. Reactive Oxygen Species as Potential Antiviral Targets. *Rev. Med. Virol.* **2022**, *32*, No. e2240.
(65) Sirelkhatim, A.; Mahmud, S.; Seeni, A.; Kaus, N. H. M.; Ann, L. C.; Bakhori, S. K. M.; Hasan, H.; Mohamad, D. Review on Zinc Oxide Nanoparticles: Antibacterial Activity and Toxicity Mechanism. *Nano-Micro Lett.* **2015**, *7*, 219−242.
(66) Wang, D.; Zhao, L.; Ma, H.; Zhang, H.; Guo, L.-H. Quantitative Analysis of Reactive Oxygen Species Photogenerated on Metal Oxide Nanoparticles and Their Bacteria Toxicity: The Role of Superoxide Radicals. *Environ. Sci. Technol.* **2017**, *51*, 10137−10145.
(67) Wang, D.; Zhu, Y.; Wan, X.; Zhang, X.; Zhang, J. Colloidal Semiconductor Nanocrystals for Biological Photodynamic Therapy Applications: Recent Progress and Perspectives. *Prog. Nat. Sci.: Mater. Int.* **2020**, *30*, 443−455.
(68) Abulikemu, M.; Tabrizi, B. E. A.; Ghobadloo, S. M.; Mofarah, H. M.; Jabbour, G. E. Silver Nanoparticle-Decorated Personal Protective Equipment for Inhibiting Human Coronavirus Infectivity. *ACS Appl. Nano Mater.* **2022**, *5*, 309−317.
(69) Park, S.; Ko, Y.-S.; Lee, S. J.; Lee, C.; Woo, K.; Ko, G. Inactivation of Influenza A Virus Via Exposure to Silver Nanoparticle-Decorated Silica Hybrid Composites. *Environ. Sci. Pollut. Res.* **2018**, *25*, 27021−27030.
(70) Medhi, R.; Srinoi, P.; Ngo, N.; Tran, H.-V.; Lee, T. R. Nanoparticle-Based Strategies to Combat COVID-19. *ACS Appl. Nano Mater.* **2020**, *3*, 8557−8580.
(71) Hou, Y.-X.; Abdullah, H.; Kuo, D.-H.; Leu, S.-J.; Gultom, N. S.; Su, C.-H. A Comparison Study of SiO_2/Nano Metal Oxide Composite Sphere for Antibacterial Application. *Composites, Part B* **2018**, *133*, 166−176.
(72) Kröger, F. A.; Vink, H. J.Relations between the Concentrations of Imperfections in Crystalline Solids. In *Solid State Physics*; Seitz, F., Turnbull, D., Eds.; Academic Press, 1956; Vol. *3*, pp 307−435.
(73) Coronavirus is in the Air - here's Too Much Focus on Surfaces. *Nature***2021**, *590* (), 7 DOI: 10.1038/d41586-021-00277-8.
(74) Behzadinasab, S.; Chin, A. W. H.; Hosseini, M.; Poon, L. L. M.; Ducker, W. A. SARS-CoV-2 Virus Transfers to Skin Through Contact with Contaminated Solids. *Sci. Rep.* **2021**, *11*, 22868.